Backscattering of topologically protected helical edge states by line defects

Mohadese Karimi, Mohsen Amini,* Morteza Soltani,† and Mozhgan Sadeghizadeh
Department of Physics, Faculty of Physics, University of Isfahan, Isfahan 81746-73441, Iran

(Received 23 July 2023; revised 20 October 2023; accepted 12 January 2024; published 25 January 2024)

The quantization of conductance in the presence of nonmagnetic point defects is a consequence of topological protection and the spin-momentum locking of helical edge states in two-dimensional topological insulators. This protection ensures the absence of backscattering of helical edge modes in the quantum Hall phase of the system. However, in this paper, we focus on exploring an approach to spoil such conductance quantization. We propose that a linear arrangement of (nonmagnetic) on-site impurities can effectively cause deviations from the conductance quantization of the edge states in the Kane-Mele model. To investigate this phenomenon, we consider an armchair ribbon containing a line defect spanning its width. Utilizing the tight-binding model and nonequilibrium Green's function method, we calculate the transmission coefficient of the system. Our results reveal a suppression of conductance at energies near the lower edge of the bulk gap for positive on-site potentials. To further comprehend this behavior, we perform analytical calculations and discuss the formation of an impurity channel. This channel arises due to the overlap of in-gap bound states, linking the bottom edge of the ribbon to its top edge, consequently facilitating backscattering. Our explanation is supported by the analysis of the local density of states at sites near the position of impurities.

DOI: 10.1103/PhysRevB.109.024108

I. INTRODUCTION

The emergence of two-dimensional (2D) topological insulators (TIs) has revolutionized the field of condensed matter physics by introducing a fascinating phenomenon known as bulk-boundary correspondence [1]. This principle dictates the existence of metallic gap states that are confined to the one-dimensional (1D) edges of the material. These edge states exhibit a distinct property of spin polarization, where the spin of an electron becomes rigidly coupled to its momentum. The intriguing consequence of this phenomenon is that electrons traveling along the edge exhibit remarkable immunity to backscattering caused by nonmagnetic defects, leading to conductance quantization. This phenomenon is known as topological edge state protection and lies at the heart of the celebrated quantum spin Hall effect [1–3].

The study of topological protection in 2D TIs raises a crucial question concerning the mechanisms that can lift this protection. This issue holds a dual significance. Firstly, it pertains to the puzzling deviations from conductance quantization observed in experiments on 2D TIs [4–6], necessitating a deeper understanding of the underlying mechanisms that induce the lifting of protection [7–9]. Secondly, in many practical scenarios, the ability to control and manipulate edge states becomes paramount [10–16]. Depending on the specific device and application, there arises a need to modulate or suppress these edge states, underscoring the importance of comprehending the mechanisms behind the lifting of protection.

So far, numerous proposals have been put forth to explain the mechanisms behind the lifting of topological protection and the subsequent occurrence of backscattering in 2D TIs. Possible sources of backscattering include mechanisms that violate time-reversal symmetry, such as the influence of an external magnetic field [17], the presence of charge puddles [18], the interaction with embedded nuclear spins [19,20], coupling to phonons [21], and the impact of electromagnetic noise [22]. However, a more direct and controllable approach for lifting topological protection is achieved through tunneling between opposite edges of a 2D TI [14–16,23–26], which enables the coupling of electrons moving in one direction with their counterparts of the same spin orientation on the opposing edge. As a result, a small gap is opened at the Fermi level [27], and more significantly, a channel for electron backscattering is created without the need to break time-reversal symmetry. A potential scenario for achieving this condition involves the creation of spatially extended defects within a 2D TI, which can be engineered through methods such as nanopatterning or the introduction of specific line defects in the atomic lattice [28].

Recently, a promising achievement in the observation of edge coupling due to the presence of an extended linear defect in a 2D TI is reported experimentally [29]. In this experimental study, bismuthene, which serves as a prototypical 2D TI, is utilized. Interestingly, it is observed that narrow constrictions spontaneously manifest themselves within the material in the form of line defects. By employing scanning tunneling microscopy/spectroscopy (STM/STS) measurements and analyzing the local density of states (LDOS), it has been discovered that the presence of the line defect leads to a spatial overlap of the edge states localized along both edges of the line defect. This spatial overlap induces a phenomenon known

*msn.amini@sci.ui.ac.ir
†mo.soltani@sci.ui.ac.ir

as hybridization, which involves the mixing of the edge states from each edge [29]. As a consequence of this hybridization, interedge scattering occurs, giving rise to a gap in the energy spectrum. The presence of this gap creates a channel through which back scattering can take place.

In this paper, we introduce a mechanism for the disruption of conductance quantization in 2D TIs. Our proposed mechanism involves the application of line defects, which results in the breakdown of conductance quantization without the need for direct coupling of edge states. Importantly, this breakdown occurs without the opening of a gap in the energy spectrum. In this paper, we focus on a 2D TI ribbon that contains a line of on-site impurities (line defect) along its longitudinal direction. Our objective is to investigate the robustness of the transport properties of the system using the nonequilibrium Green's function formalism [30]. By employing this framework, we aim to gain insights into how the presence of line defects affects the transport characteristics of the 2D TI ribbon. Utilizing a combination of numerical simulations and analytical calculations, we have discovered that the presence of the on-site potential plays a crucial role in the emergence of quasi-1D bound states along the line defect in the 2D TI ribbon. Due to the topological features of the system, the energy of the bound states remains within the gap region [31,32]. The overlap of the resulting bound states gives rise to the formation of an additional band leading to the intriguing phenomenon of transforming the line defect into a quantum wire that facilitates the transportation of current across the width of the ribbon. Moreover, the presence of the line defect introduces a mechanism for backscattering, which affects the transport properties of the system. Our findings shed light on the intricate interplay between on-site potential, line defects, and the transport behavior in 2D TI ribbons, offering insights into the manipulation and control of quantum states in these systems.

The rest of the paper is organized as follows. In Sec. II, we provide a comprehensive description of the model system under consideration and outline the methodology employed to study the transmission through this system. Moving to Sec. III, we present the results obtained from our quantum transport study of the system in the presence of the line defect. We thoroughly discuss the mechanism responsible for the breakdown of topological protection through analytical calculations, elucidating the formation of the impurity channel resulting from bound states in the bulk gap region. Finally, in Sec. IV, we conclude our findings.

II. MODEL AND METHOD

A. Model

In this section, we present a setup designed to investigate the transport properties of a 2D TI ribbon with an embedded line defect. Our device consists of two conducting leads that enclose a scattering region, as depicted in Fig. 1. The scattering region includes a line of sites with defects, which are visually represented by distinct colors in Fig. 1. As it is shown, we consider a 2D honeycomb lattice with armchair edges along the x direction. To emulate the transport through an infinitely long ribbon in the x direction, the ribbon under

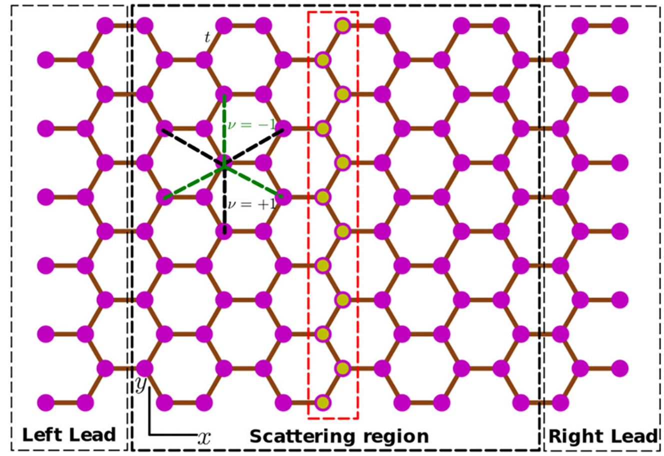

FIG. 1. Schematic representation of a two-terminal device with an infinitely long Kane-Mele ribbon with armchair boundaries connected to macroscopic leads on the left and right sides. The scattering region contains a line defect of on-site impurities arranged in a zigzag chain across the width of the ribbon (yellow circles surrounded by dashed orange rectangle). The sign of ν_{ij} for the spin-orbit coupling term is shown in the scattering region. The width of the ribbon is $W = 6$ armchair chains.

consideration in this model has a finite width W in the y direction. To achieve this, two semi-infinite leads are connected to the central region, as illustrated in Fig. 1. The Hamiltonian governing the scattering region as well as the conducting leads in the tight-binding approximation is expressed as [33,34]

$$\mathcal{H}_{\mathrm{KM}} = t \sum_{\langle i,j\rangle,\alpha} c_{i\alpha}^{\dagger} c_{j\alpha} + i\lambda_{\mathrm{SO}} \sum_{\langle\langle i,j\rangle\rangle,\alpha\beta} \nu_{ij} c_{i\alpha}^{\dagger} s_{\alpha\beta}^{z} c_{j\beta} + \mathrm{H.c.} \tag{1}$$

This Hamiltonian consists of several terms. The first term corresponds to the nearest-neighbor (NN) hopping with amplitude t, where $c_{i\alpha}^{\dagger}(c_{i\alpha})$ denotes the creation (annihilation) operator for an electron with spin α at site i. The summation $\langle i, j\rangle$ runs over all the NN sites. The second term represents the intrinsic spin-orbit coupling (SOC) with coupling strength λ_{SO} between next-NN (NNN) sites. The summation $\langle\langle i, j\rangle\rangle$ in the index indicates that it runs over all pairs of NNN sites, and the Pauli matrices $\mathbf{s} = (s^x, s^y, s^z)$ are associated with the physical spins. The factor $\nu_{ij} = \frac{\mathbf{d}_i \times \mathbf{d}_j}{|\mathbf{d}_i \times \mathbf{d}_j|} = \pm 1$ in the second term depends on the hopping path between NNN sites i and j. It is determined by the cross-product of the vectors $\mathbf{d}_i$ and $\mathbf{d}_j$ connecting the NNN sites and takes values of ± 1 as shown in Fig. 1. The term H.c. represents the Hermitian conjugate of the previous terms.

To introduce a line of noninteracting impurities, we incorporate a zigzag chain of sites spanning across the width of the ribbon in the scattering region. These sites possess an additional on-site potential V, creating a line defect indicated by a red rectangle in Fig. 1. The corresponding Hamiltonian for this line defect can be written as follows:

$$\mathcal{H}_{\mathrm{LD}} = V \sum_{i \in \mathrm{LD},\alpha} c_{i\alpha}^{\dagger} c_{i\alpha}. \tag{2}$$

B. Method

We employ the nonequilibrium Green's function formalism to investigate the electronic transport properties of our system [30]. This approach allows us to analyze the flow of electrons and calculate quantities such as the transmission coefficient and conductance. The transmission coefficient (τ) at zero temperature within this formalism can be computed using the Landauer-Buttiker formula, given by

$$\tau(E) = \mathrm{Tr}[\Gamma_L(E)G_r(E)\Gamma_R(E)G_a(E)]. \tag{3}$$

In this context, the retarded Green's function in the site representation, denoted as $G_r(E)$, is given by $G_r(E) = [E - \mathcal{H}_C - \Sigma_R(E) - \Sigma_L(E)]^{-1}$, where $\mathcal{H}_C = \mathcal{H}_{\mathrm{KM}} + \mathcal{H}_{\mathrm{LD}}$ represents the Hamiltonian of the scattering region, which incorporates the influence of the line defect. Similarly, the advanced Green's function, denoted as $G_a(E)$, is defined as the Hermitian conjugate of $G_r(E)$, i.e., $G_a(E) = [G_r(E)]^\dagger$. The self-energy terms $\Sigma_{R(L)}$ correspond to the embedding self-energy, which relies on the retarded contact Green's functions and the coupling between the leads $R(L)$ and the central (scattering) region. The right and left linewidth functions, denoted as $\Gamma_{R(L)}(E)$, can be expressed as $\Gamma_{R(L)}(E) = i\{\Sigma_{R(L)} - [\Sigma_{R(L)}]^\dagger\}$.

III. RESULTS AND DISCUSSION

In this section, we analyze the electronic transport properties of the structure mentioned above. In our calculations, we take the NN hopping amplitude t as the energy unit. Additionally, we set the width of the ribbon to be $W = 30$, a value chosen to be sufficiently large to avoid coupling of edge states [27] and fix $\lambda_{\mathrm{SO}} = 0.2t$. To numerically calculate the transmission coefficients $\tau(E)$, we will utilize the PYQULA library [35].

A. Breakdown of the conductance quantization

To begin, let us examine the band structure of the pristine system ($V = 0$), which is illustrated in Fig. 2(a). As expected, the band structure displays a bulk band gap of approximately $\Delta = 6\sqrt{3}\lambda_{\mathrm{SO}}$ [33,34], along with the presence of edge bands near the gap region. The corresponding transmission coefficient $\tau(E)$ for the edge states is depicted by the blue lines in Fig. 2(b). Notably, in the vicinity of the gap region, the transmission coefficient of the edge states is $\tau(E) = 1$, indicating their protected nature.

However, when we introduce a line defect with $V \neq 0$, the situation becomes significantly different. Our calculations reveal that, for $V = 1.0t$, the transmission coefficient of the edge states is suppressed for energies near the bottom of the bulk bands ($E \sim -0.9t$). As a consequence, this induces backscattering of the associated edge states, ultimately leading to the breakdown of conductance quantization for these states. In the subsequent analysis, we will delve into the underlying reasons for this intriguing phenomenon.

B. Analysis of the impurity channel formation

In this subsection, we will demonstrate that the deviations from quantization of the edge states transmission in the presence of the line defect can be attributed to the formation of an additional channel that connects the top edge of the ribbon to the bottom edge. Figure 3 provides a schematic representation of the transmission of helical electrons through the newly induced channel created across the line defect in the y direction. This channel facilitates the backscattering of electrons in the x direction. To address this phenomenon analytically, we will examine the in-gap impurity states, which play a crucial role in the creation of this conducting channel. To achieve this, we will begin by analyzing the in-gap impurity states of a Su-Schrieffer-Heeger (SSH) [36] model. Subsequently, we will extend and generalize these findings to our Kane-Mele ribbon. By studying the SSH model first, we can gain insights into the formation of in-gap impurity states, which will provide a foundation for our analysis of the behavior of the Kane-Mele ribbon in the presence of a line defect.

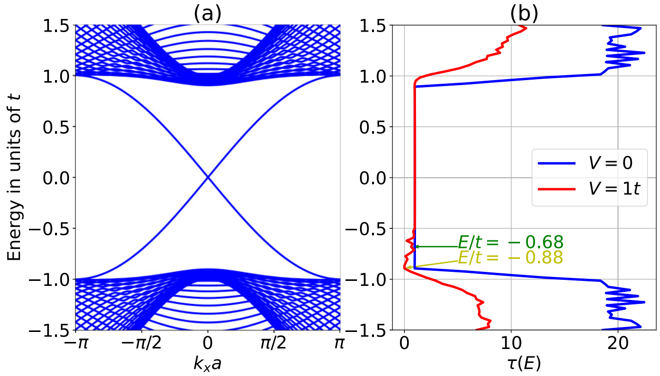

FIG. 2. (a) Electronic band structure of the pristine Kane-Mele model on a ribbon with armchair terminations and a width of $W = 30$. The spin-orbit coupling strength is $\lambda_{\mathrm{SO}} = 0.2t$. (b) The corresponding zero-temperature transmission coefficient $\tau(E)$ as a function of energy for both absence ($V = 0$) and presence ($V = 1.0$) of the line defect in the scattering region. The transmission coefficient curve demonstrates the quantization plateaus in the absence of the line defect, indicating topological protection, and the suppressed transmission regions caused by the line defect, leading to dips in the transmission coefficient curve. Two specific energy points with large and small suppression are highlighted at $E = -0.88t$ and $-0.68t$, respectively.

1. In-gap impurity state in the SSH model

In this section, we investigate an SSH chain with an on-site impurity, as depicted in Fig. 4. The SSH chain consists of two nonequivalent sites, labeled A and B, within each periodic cell. The Hamiltonian of the system is given by the sum of two

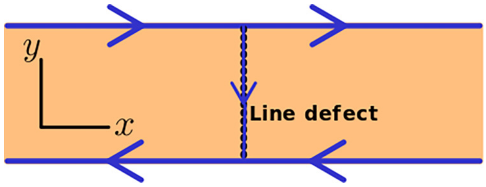

FIG. 3. Illustration of the mechanism enabling the backscattering of helical edge states that are initially moving in the x direction. It does so by utilizing the induced impurity channel created due to the presence of the line defect in the y direction.

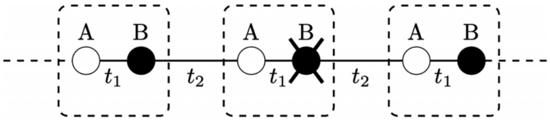

FIG. 4. The geometry of a Su-Schrieffer-Heeger (SSH) chain with two types of sublattices, labeled as A and B. The unit cell of the chain is enclosed by a dashed rectangle, and the intracell and intercell hopping amplitudes are represented by t_1 and t_2, respectively.

terms, the SSH term and the impurity term, expressed as

$$\mathcal{H} = \mathcal{H}_{\mathrm{SSH}} + \mathcal{H}_{\mathrm{impurity}}, \tag{4}$$

where

$$\mathcal{H}_{\mathrm{SSH}} = \sum_i t_1 a_i^\dagger b_i + t_2 b_i^\dagger a_{i+1} + \mathrm{H.c.}, \tag{5}$$

and

$$\mathcal{H}_{\mathrm{impurity}} = V b_0^\dagger b_0. \tag{6}$$

Here, $a_i^\dagger (a_{i+1})$ and $b_i^\dagger (b_i)$ are the creation (annihilation) operators at the corresponding sites in the unit cell, with different coupling amplitudes denoted as t_1 and t_2 for the intracell and intercell couplings, respectively. The parameter V represents the strength of the on-site impurity potential, which is considered to be located at site $i = 0$.

Let us begin by considering the case of the clean system, where $V = 0$. We are primarily interested in the bulk properties of the system, which implies considering a sufficiently long chain [37]. To analyze the bulk properties of the system in momentum space, we apply the Fourier transformation to the SSH term $\mathcal{H}_{\mathrm{SSH}}$ of Eq. (5), leading to the corresponding momentum-space Hamiltonian:

$$\mathcal{H}_{\mathrm{SSH}}(k) = \sum_k [a_k^\dagger \quad b_k^\dagger][h(k)]\begin{bmatrix} a_k \\ b_k \end{bmatrix}, \tag{7}$$

where

$$\begin{aligned} h(k) &= \begin{bmatrix} 0 & t_1 + t_2 e^{ik} \\ t_1 + t_2 e^{-ik} & 0 \end{bmatrix} \\ &= [t_1 + t_2 \cos(k)]\sigma_x + [t_2 \sin(k)]\sigma_y. \end{aligned} \tag{8}$$

In the above equation, σ_x and σ_y represent the Pauli matrices. Now the energy spectrum of $h(k)$ can be obtained by calculating its eigenvalues, which are given by

$$E^{\pm}(k) = \pm\sqrt{t_1^2 + t_2^2 + 2t_1 t_2 \cos k}. \tag{9}$$

As a result, the energy gap between the two energy bands is given by

$$E_g = 2|t_2 - t_1|. \tag{10}$$

In this model, when the intercell hopping parameter (t_1) is smaller than the intracell hopping parameter (t_2), the chain exhibits a dimerized pattern, leading to a topologically nontrivial phase characterized by a winding number (W) of 1 [37]. Conversely, when $t_1 > t_2$, the chain becomes uniform, resulting in a trivial phase with $W = 0$. We will now focus on the topologically nontrivial phase where $t_2 > t_1$ and attempt to find the end modes, also known as edge states, which satisfy the Schrödinger equation $\mathcal{H}_{\mathrm{SSH}}|\psi_{\mathrm{edge}}\rangle = 0$. Due to the chiral symmetry of the system, the corresponding edge state can be expressed in such a way that it has support on only one sublattice [37], for example, sublattice A. Therefore, we have $\langle 0|b_i|\psi_{\mathrm{edge}}\rangle = 0$, and the solution of the zero-energy eigenstate can be expressed as

$$|\psi_{\mathrm{edge}}\rangle = \sum_i \psi_i^A a_i^\dagger|0\rangle = \sum_i \left(-\frac{t_1}{t_2}\right)^i \psi_1^A a_i^\dagger|0\rangle, \tag{11}$$

where the coefficient ψ_1^A can be determined using the normalization condition as $(\psi_1^A)^2 = 1 - (\frac{t_1}{t_2})^2$.

Now let us consider the case where $V \neq 0$. We aim to demonstrate that the presence of an on-site impurity potential induces a bound state with energy E_s in the gap region $-E_g/2 < E_s < E_g/2$. To achieve this, we assume that the impurity is located on a B site, as depicted in Fig. 4. We begin by making an initial assumption about the form of the wave function associated with such an in-gap bound state as

$$|\psi_s\rangle = |\psi_A^r\rangle + |\psi_A^l\rangle + |\psi_B\rangle. \tag{12}$$

Here, $|\psi_A^r\rangle$ and $|\psi_A^l\rangle$ represent the contributions involving solely the A sublattice sites on the right and left sides, respectively, while $|\psi_B\rangle$ denotes the contribution involving solely the B sublattice sites and are defined as

$$\begin{aligned} |\psi_A^r\rangle &= \sum_{i>0} \psi_i^{A_r} a_i^\dagger|0\rangle = \sum_{i>0} \psi_1^{A_r}(-\alpha)^i a_i^\dagger|0\rangle, \\ |\psi_A^l\rangle &= \sum_{i\leqslant 0} \psi_i^{A_l} a_i^\dagger|0\rangle = \sum_{i\leqslant 0} \psi_0^{A_l}(-\alpha)^i a_i^\dagger|0\rangle, \\ |\psi_B\rangle &= \sum_i \psi_i^B b_i^\dagger|0\rangle = \sum_i \psi_0^B|-\alpha|^i b_i^\dagger|0\rangle, \end{aligned} \tag{13}$$

where $\psi_j^{A_r(A_l)}$ and ψ_j^B represent the amplitudes of the wave function on the jth site of sublattice A on the right (left) side of the impurity and on sublattice B, respectively. Indeed, the reason for considering two distinct parts, $|\psi_A^r\rangle$ and $|\psi_A^l\rangle$, in the case of the A sublattice components is due to the lack of symmetry in the wave function on the left and right sides of the impurity. The impurity introduces an asymmetry in the system, leading to different contributions from the A sublattice sites on each side. This asymmetry does not impact the B sublattice sites, as they remain invariant under the inversion symmetry relative to the location of the impurity. Therefore, to accurately describe the behavior of the wave function, we need to consider separate components for only the A sublattice sites on the right and left sides of the impurity, along with symmetric components for the B sublattice sites. Subsequently, we insert this assumed solution into the equation:

$$\mathcal{H}|\psi_s\rangle = (\mathcal{H}_{\mathrm{SSH}} + \mathcal{H}_{\mathrm{impurity}})|\psi_s\rangle = E_s|\psi_s\rangle, \tag{14}$$

enabling us to solve for the coefficients that render the equation valid. These considerations lead to the following set of equations for the amplitudes of the wave function:

$$\begin{aligned} t_1\psi_0^{A_l} + t_2\psi_1^{A_r} &= (E_s - V)\psi_0^B, \\ (t_2 - \alpha t_1)\psi_0^B &= E_s\psi_1^{A_r}, \\ (t_1 - \alpha t_2)\psi_1^{A_r} &= -\alpha E_s\psi_0^B, \end{aligned}$$

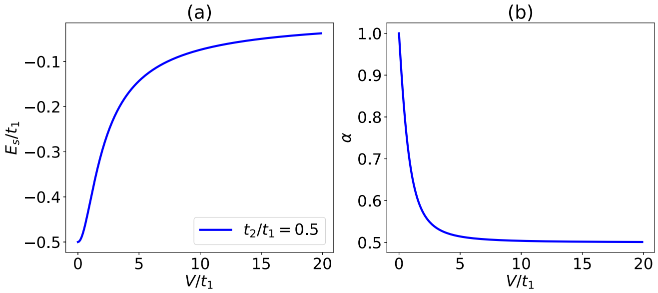

FIG. 5. Graphical representation of the solutions to the equation set in Eq. (16). In (a), we observe the variation of the bound state energy E_s (measured in units of t) as a function of the impurity potential V/t for a single impurity located on the Su-Schrieffer-Heeger (SSH) chain with $t_2/t_1 = 0.5$. Notably, for extremely large values of the on-site potential, the bound state energy tends to zero, which aligns with the energy of the edge states in the system. (b) illustrates the corresponding coefficient α, as defined in the equation set in Eq. (13).

$$(t_1 - \alpha t_2)\psi_0^B = E_s \psi_0^{A_l},$$
$$(t_2 - \alpha t_1)\psi_0^{A_l} = -\alpha E_s \psi_0^B. \tag{15}$$

In addition to the three unknown amplitudes of the wave function $\psi_0^{A_l}$, $\psi_1^{A_r}$, and ψ_0^B, we have two additional unknown quantities, namely, E_s and α. Before starting to solve this set of equations, it is noteworthy that altering the hopping amplitudes t_1 and t_2 interchangeably, along with switching the r and l labels of the components of the wave functions, does not alter the form of the equations in Eq. (15). Such invariants in the equations are expected due to the symmetry properties of the system and only hold when we consider symmetric components of the wave functions on sites belonging to sublattice B, as discussed earlier. To determine E and α, we need to solve the set of five equations. However, our main interest lies in finding E_s and α directly. Therefore, we can eliminate the other three unknowns from the equations through some algebraic manipulations, resulting in the following expressions:

$$t_1 T_1 + t_2 T_2 = E_s(E_s - V),$$
$$T_1 T_2 = -\alpha E_s^2. \tag{16}$$

Here, we have defined $T_1 = t_1 - \alpha t_2$ and $T_2 = t_2 - \alpha t_1$. By solving these two equations, we can obtain the desired values of E_s and α. This set of equations has two sets of solutions: one with E_s inside the gap region and the other with E_s outside. The first set exhibits the following structure:

$$E_s = -\sqrt{\frac{V^2}{2} + t_1^2 + t_2^2 - \frac{\sqrt{V^4 + 4V^2 t_1^2 + 4V^2 t_2^2 + 16 t_1^2 t_2^2}}{2}}, \tag{17}$$

and

$$\alpha = \frac{-\frac{V^2}{2} + V E_s + \frac{\sqrt{V^4+4V^2t_1^2+4V^2t_2^2+16t_1^2t_2^2}}{2}}{2t_1 t_2}, \tag{18}$$

which is shown graphically in Fig. 5. As shown, regardless of the strength of the impurity potential V, a bound state emerges within the energy gap. For extremely large values of V ($V \to \infty$), the energy of the bound state approaches zero ($E_s/t_1 \to 0$), and the value of α converges to $\frac{t_2}{t_1}$. As we decrease the impurity strength V, the energy of the bound state gradually decreases until it eventually merges with the bulk states at $V = 0$.

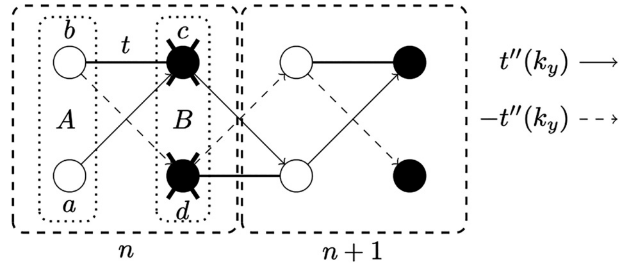

FIG. 6. Schematic representation of the two-leg ladder model, obtained through a dimensional reduction procedure outlined in Ref. [38], for the Kane-Mele ribbon. The unit cell of the model consists of four sites (labeled a, b, c, and d) denoted by a dashed rectangle, forming a plaquette. Following the analogy with the Su-Schrieffer-Heeger (SSH) chain, each plaquette is divided into two blocks, A and B, shown by dotted lines, with each block containing two sites. The hopping parameters $t''(k_y)$ and $-t''(k_y)$ are indicated by solid and dashed vectors, respectively, and are defined as $t''(k_y) = 2\lambda_{SO}\sin(\frac{k_y}{2})$.

2. *Generalization of the analysis for the Kane-Mele ribbon embedded with a line defect*

We can extend the previous calculations to the case of a Kane-Mele ribbon with a line defect along the y direction, as illustrated in Fig. 1. To simplify the analysis, we assume that the ribbon is wide enough along the y direction so that the momentum k_y can be treated as a good quantum number. This assumption allows us to employ the method and notation introduced in Ref. [38], where the Kane-Mele Hamiltonian of Eq. (1) is mapped onto a two-leg ladder system with a generalized SSH Hamiltonian in the k_y space, $\mathcal{H}_{KM}(k_y) = \mathcal{H}_0(k_y) + \mathcal{H}_1(k_y)$. In this ladder model, the unit cell consists of a plaquette composed of four sites, denoted as a, b, c, and d. To establish an analogy with the SSH chain, we label the sites a and b as block A and the sites c and d as block B, as depicted in Fig. 6. In this notation, the transformed Hamiltonian for the ladder system consists of two terms $\mathcal{H}_0(k_y)$ and $\mathcal{H}_1(k_y)$. Here, $\mathcal{H}_0(k_y)$ represents a zero-energy flat band, while $\mathcal{H}_1(k_y)$ is responsible for the dispersion of the edge band. To proceed, we first aim to obtain the impurity bound state for the ladder system in the absence of $\mathcal{H}_1(k_y)$. A schematic representation of this ladder system is depicted in Fig. 6, and we can write the Hamiltonian $\mathcal{H}_0(k_y)$ as follows [27]:

$$\mathcal{H}_0(k_y) = \sum_n [a_n^\dagger b_n^\dagger]\widehat{t_1}\begin{bmatrix} c_n \\ d_n \end{bmatrix} + \sum_n [c_n^\dagger d_n^\dagger]\widehat{t_2}\begin{bmatrix} a_{n+1} \\ b_{n+1} \end{bmatrix} + \text{H.c.}, \tag{19}$$

where

$$\widehat{t_1} = \begin{bmatrix} t & -t'(k_y) \\ t'(k_y) & 0 \end{bmatrix}, \tag{20}$$

$$\widehat{t_2} = \begin{bmatrix} 0 & t'(k_y) \\ -t'(k_y) & t \end{bmatrix}, \tag{21}$$

where $t'(k_y) = 2\lambda_{\text{SO}} \sin(\frac{k_y}{2})$ and the summation on n runs over all the plaquettes in the ladder model.

In the presence of the line defect, the Hamiltonian given by Eq. (2) alters the on-site potential of the corresponding block of the ladder system (based on the location of the defected zigzag chain) to the on-site energy V. For instance, in Fig. 6, the line defect is shown on block B of the nth plaquette. Thus, there exists an analogy between the SSH ladder and SSH chain, and we can derive the corresponding set of equations given in Eq. (15) for the ladder system by simply replacing the wave function amplitudes in the SSH chain model as two-component vectors. That is, $|\psi^{A_r}\rangle = [\begin{smallmatrix}\psi^{a_r}\\ \psi^{b_r}\end{smallmatrix}]$, $|\psi^{A_l}\rangle = [\begin{smallmatrix}\psi^{a_l}\\ \psi^{b_l}\end{smallmatrix}]$, and $|\psi^{B}\rangle = [\begin{smallmatrix}\psi^{c}\\ \psi^{d}\end{smallmatrix}]$. This immediately results in the following set of equations:

$$\begin{aligned}
\widehat{t_1}^\dagger \begin{bmatrix}\psi_0^{a_l}\\ \psi_0^{b_l}\end{bmatrix} + \widehat{t_2}\begin{bmatrix}\psi_1^{a_r}\\ \psi_1^{b_r}\end{bmatrix} &= (E_s - V)\begin{bmatrix}\psi_0^{c}\\ \psi_0^{d}\end{bmatrix},\\
(\widehat{t_2}^\dagger - \alpha\widehat{t_1})\begin{bmatrix}\psi_0^{c}\\ \psi_0^{d}\end{bmatrix} &= E_s\begin{bmatrix}\psi_1^{a_r}\\ \psi_1^{b_r}\end{bmatrix},\\
(\widehat{t_1}^\dagger - \alpha\widehat{t_2})\begin{bmatrix}\psi_1^{a_r}\\ \psi_1^{b_r}\end{bmatrix} &= -\alpha E_s\begin{bmatrix}\psi_0^{c}\\ \psi_0^{d}\end{bmatrix},\\
(\widehat{t_1} - \alpha\widehat{t_2}^\dagger)\begin{bmatrix}\psi_0^{c}\\ \psi_0^{d}\end{bmatrix} &= E_s\begin{bmatrix}\psi_0^{a_l}\\ \psi_0^{b_l}\end{bmatrix},\\
(\widehat{t_2} - \alpha\widehat{t_1}^\dagger)\begin{bmatrix}\psi_0^{a_l}\\ \psi_0^{b_l}\end{bmatrix} &= -\alpha E_s\begin{bmatrix}\psi_0^{c}\\ \psi_0^{d}\end{bmatrix}.
\end{aligned} \tag{22}$$

By the same token, this will allow us to obtain the unknown quantities $E_s(k_y)$ and $\alpha(k_y)$ through the solution of the following equations:

$$\begin{aligned}
\widehat{t_1}^\dagger \widehat{T_1} + \widehat{t_2}\widehat{T_2} &= E_s(E_s - V)\widehat{I},\\
\widehat{T_1}\widehat{T_2}^\dagger &= -\alpha E_s^2 \widehat{I},
\end{aligned} \tag{23}$$

where $\widehat{T_1} = \widehat{t_2}^\dagger - \alpha\widehat{t_1}$ and $\widehat{T_2} = \widehat{t_1}^\dagger - \alpha\widehat{t_2}$. By applying the same approach, we can determine the solution set for the aforementioned equations and identify the solution within the energy gap as

$$E_s = -\sqrt{\frac{V^2}{2} + t^2 + 2t'^2 - \frac{\sqrt{V^4 + 4V^2t^2 + 8V^2t'^2 + 16t'^4}}{2}}, \tag{24}$$

and

$$\alpha = -\frac{\frac{V^2}{2} - VE_s - \frac{\sqrt{V^4+4V^2t^2+8V^2t'^2+16t'^4}}{2}}{2t'^2}. \tag{25}$$

The derived expression for the energy of bound states in Eq. (24) explicitly depends on the wave number k_y and introduces an extra energy band within the gap region, as visually

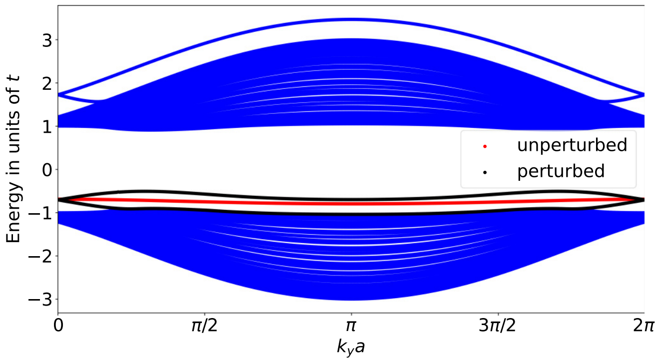

FIG. 7. Visual representation of the doubly degenerate dispersion relation of the impurity band described in Eq. (24). This band is formed through the overlapping of bound states emerging within the gap region of the armchair Kane-Mele model, where the on-site potential is $V = 1.0t$ and $\lambda_{\text{SO}} = 0.2t$. The unperturbed impurity band is depicted in red, while the perturbed impurity band is shown in black, and the edge bands have not been shown to avoid confusion.

represented in Fig. 7 which is highlighted in red. This observation indicates the formation of an impurity band [39], which leads to the creation of an impurity channel responsible for the coupling between the top and bottom edges of the ribbon. Lastly, it is worth mentioning that the impurity band derived from Eq. (24) exhibits a twofold energy degeneracy. To resolve this twofold energy degeneracy, one should consider the effect of $\mathcal{H}_1(k_y)$. To address this twofold energy degeneracy, it is necessary to consider the influence of $\mathcal{H}_1(k_y)$. This can be achieved by applying first-order perturbation theory, following the approach outlined in Ref. [38]. However, the resulting energy dispersion is too intricate to be presented analytically; we will illustrate the final results numerically in Fig. 7. The splitting of the twofold degeneracy for the case of $\lambda_{\text{SO}} = 0.2t$ and $V = 1.0t$ is visually presented in Fig. 7. We have highlighted these in-gap impurity bands using black colors for clarity. The edge bands are not shown in the plot to avoid confusion and better focus on the behavior of the impurity bands.

Before closing this subsection, it is important to note that the variations seen in the conductance quantization of edge transport in the inverted quantum-well junctions, as reported in Refs. [40,41], differ from our observations. In our case, there is no shift in the local band structure; instead, an additional band is formed which is responsible for the resulting backscattering of the edge modes.

C. Impurity channel analysis

Another approach to comprehend the formation of the impurity channel is by investigating the LDOS at energies where topological protection is broken. By analyzing the LDOS, which is related to the matrix elements of the retarded Green's function as $\rho_i(E) = -\frac{1}{\pi}\text{Im}[\langle i|G_r(E)|i\rangle]$, we can gain insights into how the presence of the impurity potential affects the electronic states in real space and leads to the emergence of the impurity channel. Figure 8 displays the spatial distribution of the LDOS for the scattering region depicted in Fig. 1 near the line defects at energies specified in Fig. 2.

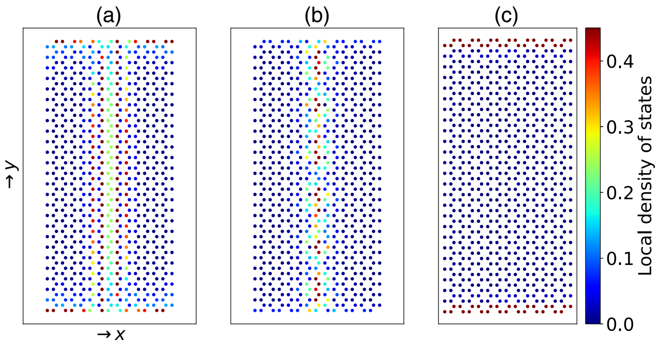

FIG. 8. Spatial profiles of the local density of states on sites adjacent to the line defect at energies specified in Fig. 2. The scattering region is a Kane-Mele ribbon (depicted in Fig. 1) with a width of $W = 26$ and spin-orbit coupling $\lambda_{SO} = 0.2t$ that hosts a line defect with on-site potential strength $V = 1.0t$. (a) Local density of states (LDOS) at energy $E/t = -0.88$ with complete suppression of the transmission coefficient. (b) LDOS at energy $E/t = -0.68$ with partial suppression of the transmission coefficient. (c) LDOS at $E/t = 0.0$ with an unchanged transmission coefficient.

We are interested in the energies near the lower gap edge where the presence of line defects has a visible impact. As before, we consider the parameters $\lambda_{SO} = 0.2t$ and $V = 1.0t$ for our calculations. These values remain consistent with our previous analysis and investigations of the behavior of the system in the presence of the line defect. Specifically, Fig. 8(a) illustrates the LDOS map at a specific energy value of $E/t = -0.88$, showcasing a complete suppression of transmission, indicating the formation of the impurity channel. Additionally, Fig. 8(b) depicts the LDOS at $E/t = -0.68$, where the transmission is not entirely suppressed, however, due to the presence of the impurity channel connecting the top and bottom edges of the ribbon partial backscattering existence. For comparison, Fig. 8(c) shows the LDOS at $E/t = 0.0$, which exclusively displays only the presence of edge states (without formation of any impurity channel), as anticipated. These results provide valuable insights into the impact of the line defect on the transmission of the edge states and the formation of the impurity channel in the system.

IV. CONCLUDING REMARKS

In summary, we have conducted an investigation into the effects of a line defect, characterized by on-site impurities arranged in a zigzag chain that connects the top and bottom edges of the Kane-Mele armchair ribbon. Our findings reveal that the presence of this line defect significantly disrupts the conductance quantization of the edge states, resulting in the backscattering of helical electrons. Consequently, the conductance of the system becomes lower than that of the pristine ribbon. To understand the mechanism underlying this backscattering phenomenon, we analyzed the bound states that emerge within the gap region of the system. Our analysis showed that, due to the overlap of localized wave functions around the impurities, an additional impurity band forms within the gap region. The primary outcome of this paper is the identification of the role of the line defect in inducing an impurity channel that spans the width of the ribbon. This impurity channel effectively facilitates the backscattering of helical electrons, leading to a suppression of quantized transmission within specific energy windows.

ACKNOWLEDGMENTS

We extend our sincere gratitude to the office of graduate studies at the University of Isfahan for their generous support and for providing us with research facilities, which were instrumental in carrying out this study. Additionally, M.A. would like to acknowledge the support received from the Abdus Salam (ICTP) associateship program.

[1] M. Z. Hasan and C. L. Kane, Colloquium: Topological insulators, Rev. Mod. Phys. **82**, 3045 (2010).
[2] X.-L. Qi and S.-C. Zhang, Topological insulators and superconductors, Rev. Mod. Phys. **83**, 1057 (2011).
[3] D. Culcer, A. C. Keser, Y. Li, and G. Tkachov, Transport in two-dimensional topological materials: Recent developments in experiment and theory, 2D Mater. **7**, 022007 (2020).
[4] S. Wu, V. Fatemi, Q. D. Gibson, K. Watanabe, T. Taniguchi, R. J. Cava, and P. Jarillo-Herrero, Observation of the quantum spin Hall effect up to 100 Kelvin in a monolayer crystal, Science **359**, 76 (2018).
[5] L. Lunczer, P. Leubner, M. Endres, V. L. Muller, C. Brune, H. Buhmann, and L. W. Molenkamp, Approaching quantization in macroscopic quantum spin Hall devices through gate training, Phys. Rev. Lett. **123**, 047701 (2019).
[6] C.-H. Hsu, P. Stano, J. Klinovaja, and D. Loss, Helical liquids in semiconductors, Semicond. Sci. Technol. **36**, 123003 (2021).
[7] L. Vannucci, T. Olsen, and K. S. Thygesen, Conductance of quantum spin Hall edge states from first principles: The critical role of magnetic impurities and inter-edge scattering, Phys. Rev. B **101**, 155404 (2020).
[8] L. R. F. Lima and C. Lewenkopf, Breakdown of topological protection due to nonmagnetic edge disorder in two-dimensional materials in the quantum spin Hall phase, Phys. Rev. B **106**, 245408 (2022).
[9] P. Novelli, F. Taddei, A. K. Geim, and M. Polini, Failure of conductance quantization in two-dimensional topological insulators due to nonmagnetic impurities, Phys. Rev. Lett. **122**, 016601 (2019).
[10] B. Jäck, Y. Xie, B. A. Bernevig, and A. Yazdani, Observation of backscattering induced by magnetism in a topological edge state, Proc. Natl. Acad. Sci. USA **117**, 16214 (2020).
[11] J. L. Collins, A. Tadich, W. Wu, L. C. Gomes, J. N. B. Rodrigues, C. Liu, J. Hellerstedt, H. Ryu, S. Tang, S.-K. Mo *et al.*, Electric-field-tuned topological phase transition in ultrathin Na_3Bi, Nature (London) **564**, 390 (2018).
[12] X. Qian, J. Liu, L. Fu, and J. Li, Quantum spin Hall effect in two-dimensional transition metal dichalcogenides, Science **346**, 1344 (2014).
[13] W. Vandenberghe and M. Fischetti, Imperfect two-dimensional topological insulator field-effect transistors, Nat. Commun. **8**, 14184 (2017).

[14] V. Krueckl and K. Richter, Switching spin and charge between edge states in topological insulator constrictions, Phys. Rev. Lett. **107**, 086803 (2011).

[15] R. P. Maciel, A. L. Araújo, C. H. Lewenkopf, and G. J. Ferreira, Fabry-Pérot resonant vortices and magnetoconductance in topological insulator constrictions with magnetic barriers, Phys. Rev. B **103**, 205124 (2021).

[16] H. Ishida and A. Liebsch, Engineering edge-state currents at the interface between narrow ribbons of two-dimensional topological insulators, Phys. Rev. Res. **2**, 023242 (2020).

[17] M. Konig, S. Wiedmann, C. Brune, A. Roth, H. Buhmann, L. W. Molenkamp, X.-L. Qi, and S.-C. Zhang, Quantum spin Hall insulator state in HgTe quantum wells, Science **318**, 766 (2007).

[18] J. I. Vayrynen, M. Goldstein, and L. I. Glazman, Helical edge resistance introduced by charge puddles, Phys. Rev. Lett. **110**, 216402 (2013).

[19] C.-H. Hsu, P. Stano, J. Klinovaja, and D. Loss, Effects of nuclear spins on the transport properties of the edge of two-dimensional topological insulators, Phys. Rev. B **97**, 125432 (2018).

[20] A. A. Bagrov, F. Guinea, and M. I. Katsnelson, Suppressing backscattering of helical edge modes with a spin bath, Phys. Rev. B **100**, 195426 (2019).

[21] J. C. Budich, F. Dolcini, P. Recher, and B. Trauzettel, Phonon-induced backscattering in helical edge states, Phys. Rev. Lett. **108**, 086602 (2012).

[22] J. I. Vayrynen, D. I. Pikulin, and J. Alicea, Noise-induced backscattering in a quantum spin Hall edge, Phys. Rev. Lett. **121**, 106601 (2018).

[23] B. Zhou, H.-Z. Lu, R.-L. Chu, S. Q. Shen, and Q. Niu, Finite size effects on helical edge states in a quantum spin-Hall system, Phys. Rev. Lett. **101**, 246807 (2008).

[24] F. Romeo, R. Citro, D. Ferraro, and M. Sassetti, Electrical switching and interferometry of massive Dirac particles in topological insulator constrictions, Phys. Rev. B **86**, 165418 (2012).

[25] Y. Takagaki, Backscattering from width variations in quasi-one-dimensional strips of topological insulators, J. Phys. Condens. Matter **24**, 435301 (2012).

[26] Y. Takagaki, Strong reflection and periodic resonant transmission of helical edge states in topological-insulator stub-like resonators, J. Appl. Phys. **118**, 054304 (2015).

[27] M. Sadeghizadeh, M. Soltani, and M. Amini, Rigorous analysis of the topologically protected edge states in the quantum spin Hall phase of the armchair ribbon geometry, Sci. Rep. **13**, 12844 (2023).

[28] E. N. Lima, T. Schmidt, and R. W. Nunes, Topologically protected metallic states induced by a one-dimensional extended defect in the bulk of a 2D topological insulator, Nano Lett. **16**, 4025 (2016).

[29] R. Stühler, A. Kowalewski, F. Reis, D. Jungblut, F. Dominguez, B. Scharf, G. Li, J. Schafer, and E. M. Hankiewicz, and R. Claessen, Effective lifting of the topological protection of quantum spin Hall edge states by edge coupling Nat. Commun. **13**, 3480 (2022).

[30] S. Datta, *Electronic Transport in Mesoscopic Systems* (Cambridge University Press, Cambridge, 1995).

[31] R.-J. Slager, L. Rademaker, J. Zaanen, and L. Balents, Impurity-bound states and Green's function zeroes as local signatures of topology, Phys. Rev. B **92**, 085126 (2015).

[32] S. S. Diop, L. Fritz, M. Vojta, and S. Rachel, Impurity bound states as detectors of topological band structures revisited, Phys. Rev. B **101**, 245132 (2020).

[33] C. L. Kane and E. J. Mele, Z_2 topological order and the quantum spin Hall effect, Phys. Rev. Lett. **95**, 146802 (2005).

[34] C. L. Kane and E. J. Mele, Quantum spin Hall effect in graphene, Phys. Rev. Lett. **95**, 226801 (2005).

[35] PYQULA Library, https://github.com/joselado/pyqula.

[36] W. P. Su, J. R. Schrieffer, and A. J. Heeger, Solitons in polyacetylene Phys. Rev. Lett. **42**, 1698 (1979).

[37] J. K. Asboth, L. Oroszlany, and A. Palyi, *A Short Course on Topological Insulators: Band Structure and Edge States in One and Two Dimensions* (Springer, Cham, 2016).

[38] F. Rahmati, M. Amini, M. Soltani, and M. Sadeghizadeh, Explicit derivation of the chiral and generic helical edge states for the Kane-Mele model: Closed expressions for the wave function, dispersion relation, and spin rotation, Phys. Rev. B **107**, 205408 (2023).

[39] M. Rezaei, H. Karbaschi, M. Amini, M. Soltani, and G. Rashedi, Thermoelectric properties of armchair phosphorene nanoribbons in the presence of vacancy-induced impurity band, Nanotechnology **32**, 375704 (2021).

[40] D. Nanclares, L. R. F. Lima, C. H. Lewenkopf, and L. G. G. V. Dias da Silva, Tunable spin-polarized edge transport in inverted quantum-well junctions, Phys. Rev. B **96**, 155302 (2017).

[41] G. M. Gusev, A. D. Levin, Z. D. Kvon, N. N. Mikhailov, and S. A. Dvoretsky, Quantum Hall effect in $n-p-n$ and n-2D topological insulator-n junctions, Phys. Rev. Lett. **110**, 076805 (2013).